scientific reports

Check for updates

OPEN

Controlled synthesis of various Fe_2O_3 morphologies as energy storage materials

Bui Thi Hang✉ & Trinh Tuan Anh

Air pollution from vehicle emissions is a major problem in developing countries. Consequently, the use of iron-based rechargeable batteries, which is an effective method of reducing air pollution, have been extensively studied for electric vehicles. The structures and morphologies of iron particles significantly affect the cycle performance of iron-based rechargeable batteries. The synthesis parameters for these iron materials also remarkably influence their structures, shapes, sizes, and electrochemical properties. In this study, we fabricated α-Fe_2O_3 materials with various shapes and sizes via a facile hydrothermal route and investigated the effects of raw materials on their structures, morphologies, and properties. The structural characteristics of the synthesized iron oxides were studied via X-ray diffraction using scanning electron microscopy. Results indicate that changing the concentration of raw materials modified the structure and morphology of the synthesized α-Fe_2O_3 particles, that is, the desired shape and size of α-Fe_2O_3 can be controlled. The effects of the structure and morphology of α-Fe_2O_3 particles on their electrochemical characteristics were investigated. The results show that the morphology and shape of the iron oxide particles remarkably affected the redox reaction rate and discharge capacity of the Fe_2O_3/C composite electrodes. Among the synthesized α-Fe_2O_3 materials, the cubic-shaped α-Fe_2O_3 exhibited the highest discharge capacity. This material is a potential candidate for application in iron-based aqueous batteries. Our results may facilitate not only the controlled synthesis of α-Fe_2O_3 nanoparticles for potential technical applications but also the production of electrode materials with high capacity and good cycle performance for iron-based rechargeable batteries.

Metal–air batteries have attracted the attention of researchers because they have a high theoretical energy, are environment-friendly, and cost lower than lithium-ion batteries[1–5]. Among the metal–air batteries, iron–air batteries are the most valued because iron has high theoretical specific energy and low cost and is abundant on earth and often non-toxic[6–10]. However, the actual energy of iron–air batteries has remained low due the limitations of iron electrodes, such as large overpotential, the passivation caused by the iron hydroxide formed during discharge, and low coulombic efficiency. In addition, hydrogen evolves simultaneously with reduction reaction of iron lowers the charging efficiency results in loss of water from the electrolyte[11–13].

In aqueous alkaline solution, two plateaus can be observed in the discharge process. The first plateau at = − 0.975 V versus Hg/HgO corresponds to the oxidation of iron to $Fe(OH)_2$. The second plateau at − 0.758 V versus Hg/HgO or − 0.658 V versus Hg/HgO corresponds to the further oxidation of $Fe(OH)_2$ to Fe(III). Iron (III) can be formed as Fe_3O_4, FeOOH, and/or Fe_2O_3[11,14,15]:

$$Fe + 2OH^- \leftrightarrow Fe(OH)_2 + 2e^-, E_o = -0.975 \text{ V versus Hg/HgO}, \quad (1)$$

$$3Fe(OH)_2 + 2OH^- \leftrightarrow Fe_3O_4 + 4H_2O + 2e^-, E_o = -0.758 \text{ V versus Hg/HgO}, \quad (2)$$

and/or

$$Fe(OH)_2 + OH^- \leftrightarrow FeOOH + H_2O + e^-, E_o = -0.658 \text{ V versus Hg/HgO}. \quad (3)$$

The low electrical conductivity of the iron oxides formed during the discharge processes can result in the low coulombic efficiency of iron electrodes.

The hydrogen evolution reaction is expressed as follows:

International Training Institute for Materials Science, Hanoi University of Science and Technology, No. 1, Dai Co Viet Road, Hanoi, Viet Nam. ✉email: hang@itims.edu.vn

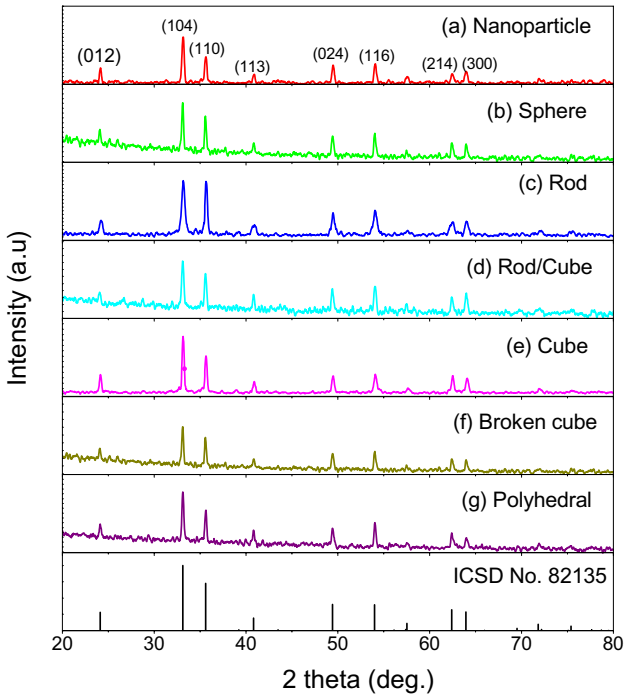

Figure 1. XRD patterns of α-Fe_2O_3 synthesized via hydrothermal route at various concentration ratios of $FeCl_3$ and cetyltrimethylammonium bromide (CTAB) (C_{FeCl_3}/C_{CTAB}): (**a**) C_{FeCl_3}/C_{CTAB} = 0.02/0.0, (**b**) 0.02/0.01, (**c**) 0.05/0.01, (**d**) 0.05/0.02, (**e**) 0.05/0.04, (**f**) 0.07/0.04, (**g**) 0.03/0.04.

$$2H_2O + 2e^- \leftrightarrow H_2 + 2OH^-, E_o = -0.926 \text{ V versus Hg/HgO}. \quad (4)$$

The standard reduction potential of the hydrogen evolution in alkaline electrolyte (Eq. 4) is slightly more positive than that of the iron electrode reaction (Eq. 1). Hydrogen evolution is possible even at open circuit on an iron electrode in alkaline solution. Consequently, hydrogen evolution (Eq. 4) occurs during charging (Eq. 1) in addition to the reduction in the iron electrode. Simultaneous hydrogen evolution can result in low faradaic efficiency during charging.

Previous studies[16–20] reported the following reactions of Fe_2O_3 electrodes in alkaline solution at the first charge:

$$Fe_2O_3 + 3H_2O + 2e^- \rightarrow 2Fe(OH)_2 + 2OH^-, \quad (5)$$

and

$$Fe(OH)_2 + 2e^- \rightarrow Fe + 2OH^-. \quad (6)$$

The composition and structure of iron electrodes have been modified to address their limitations. Furthermore, some additives for electrodes and/or electrolyte solutions are used to increase the redox reaction rate and reduce the rate of hydrogen evolution, resulting in the improved capacity and efficiency of iron electrodes[21–29]. However, the limitations of iron electrodes have not been overcome completely, so more investigations are needed. Previous studies have shown that the structure and morphology of iron particles strongly influence their electrochemical properties in alkaline solutions[24–32]. In the present study, we synthesized α-Fe_2O_3 materials with various structures and morphologies using a hydrothermal route to find the most suitable material for iron-based aqueous batteries. The desired shape and size of α-Fe_2O_3 particles were controlled by changing the concentration of raw materials and the hydrothermal parameters. Furthermore, we applied additives to the electrolyte to further improve the capacity and cycle performance of iron electrodes.

Results and discussion

Figure 1 shows the X-ray patterns of the as-prepared materials. The patterns of all the samples exhibit some typical diffraction peaks at 2 theta values of 24.17°, 33.19°, 35.66°, 40.9°, 49.51°, 54.13°, 62.49°, and 64.05°, which respectively correspond to the (012), (104) (110), (113), (024), (116), (214), and (300) planes. All the peaks can be easily indexed to hematite α-Fe_2O_3 and are consistent with the reported values in ICSD No. 82135. No other peaks for impurities can be observed in the XRD patterns. This result confirms that the synthesized products are pure α-Fe_2O_3.

From the Scherer equation, the mean size of hematite α-Fe_2O_3 crystallites is calculated, and the results are shown in Table 1. The concentration ratio of iron chloride and the CTAB surfactant (C_{FeCl_3}/C_{CTAB}) affects the average size of hematite crystallites. Without the CTAB (C_{FeCl_3}/C_{CTAB} = 0.02/0.0), the mean size of hematite

No.	Sample names	Concentration ratios of precursors (C_{FeCl_3}/C_{CTAB})	Mean size of the hematite crystallites
1	Nanoparticle	$C_{FeCl_3}/C_{CTAB} = 0.02/0.0$	29.04
2	Sphere	$C_{FeCl_3}/C_{CTAB} = 0.02/0.01$	36.36
3	Rod	$C_{FeCl_3}/C_{CTAB} = 0.05/0.01$	20.52
4	Rod/Cube	$C_{FeCl_3}/C_{CTAB} = 0.05/0.02$	30.68
5	Cube	$C_{FeCl_3}/C_{CTAB} = 0.05/0.04$	33.08
6	Broken cube	$C_{FeCl_3}/C_{CTAB} = 0.07/0.04$	36.41
7	Polyhehral	$C_{FeCl_3}/C_{CTAB} = 0.03/0.04$	35.36

Table 1. Concentration ratios of precursors, mean size of the hematite crystallites synthesized via hydrothermal route.

crystallites is approximately 29 nm (Fig. 1a). Using the CTAB with $C_{CTAB} = 0.01M$, if $C_{FeCl_3} = 0.02M$ (C_{FeCl_3}/C_{CTAB}=0.02/0.01) (Fig. 1b), the mean size of hematite crystallites increases. However, if enhancing the concentration of $FeCl_3$ to 0.05 M, the mean size of hematite crystallites decreases (Fig. 1c). The mean size of hematite crystallites increases when $C_{FeCl_3} = 0.05M$ is maintained and the CTAB amount is increased to 0.02 M or 0.04 M, that is, $C_{FeCl_3}/C_{CTAB} = 0.05/0.02$ (Fig. 1d) or $C_{FeCl_3}/C_{CTAB} = 0.05/0.04$ (Fig. 1e). Similarly, the mean size of hematite crystallites increases when $C_{CTAB} = 0.04M$ is maintained and the concentration of iron chloride is increased or decreased, that is, $C_{FeCl_3}/C_{CTAB} = 0.07/0.04$ (Fig. 1f) or $C_{FeCl_3}/C_{CTAB} = 0.03/0.04$ (Fig. 1g). Thus, the concentrations of iron chloride and the CTAB surfactant affect the mean size of hematite crystallites. The synthesized α-Fe_2O_3 hematite crystallites are polycrystalline materials whose particles contain several crystals.

The SEM images of the α-Fe_2O_3 materials synthesized at various concentration ratios of $FeCl_3$ and CTAB are shown in Fig. 2. All the samples were prepared under the same hydrothermal conditions, namely, at 120 °C for 14 h and a pH value of 10 in a typical hydrothermal process, but the concentration ratio of precursors $FeCl_3$ and CTAB (C_{FeCl_3}/C_{CTAB}) was changed to obtain Fe_2O_3 materials with different morphologies, shapes, and sizes.

In this study, CTAB acts as a cationic surfactant during synthesis. Thus, the CTAB amount affects the morphological characteristics of the synthesized iron oxides. Furthermore, the concentration of iron chloride also affects the morphology of the obtained iron oxides. By adjusting the concentration ratio of C_{FeCl_3}/C_{CTAB} in the reaction solution, different morphologies of α-Fe_2O_3 nanoparticles can be obtained. Pu et al.[33] showed that the α-Fe_2O_3 formation in the hydrothermal process may proceed through two steps. First, Fe^{3+} is hydrolyzed in aqueous solution to form the β-FeOOH precursor. Second, the resulting β-FeOOH undergoes topotactic transformation to α-Fe_2O_3 via the dissolution/reprecipitation mechanism. They demonstrated that the morphologies of the β-FeOOH precursors change continuously from nanosphere, nanorod, to nanoraft with the increase of the $FeCl_3$ concentration under the confinement of surfactants.

Figure 2a presents the sample prepared with C_{FeCl_3}= 0.02 M without CTAB ($C_{FeCl_3}/C_{CTAB} = 0.02/0.0$) is nanostructured particles, free shape, non-uniform with diameters from a few hundred nanometers to one micrometer. When $C_{CTAB} = 0.01M$ and $C_{FeCl_3} = 0.02M$ (C_{FeCl_3}/C_{CTAB}=0.02/0.01) (Fig. 2b), sphere-shaped iron oxides are formed with diameters less than 200 nm. When $C_{CTAB} = 0.01M$ and the iron chloride amount is increased to 0.05 M, that is, $C_{FeCl_3}/C_{CTAB} = 0.05/0.01$, the product comprises rod-like nanoparticles (Fig. 2c). The diameters of the α-Fe_2O_3 nanorods are approximately 50 nm, and their lengths range from 100 to 200 nm. When $C_{FeCl_3} = 0.05M$ and the CTAB concentration is increased to $C_{CTAB} = 0.02M$, nanorods aggregate and thus form some nanocubes in the product (Fig. 2d). Notably, when $C_{CTAB} = 0.04M$, perfect cubic-shaped structures are observed in the sample (Fig. 2e), but their dimensions are not uniform, with edges of a few hundred nanometers to one micrometer. Thus, when C_{FeCl_3} is low at $C_{CTAB} = 0.01M$, the product mainly consists of zero-dimensional nanoparticles, such as nanospheres (Fig. 2b). According to Pu et al.[33], the precursors in this case might be sphere-like particles of several nanometers. The shapes of the synthesized products turn to rods (Fig. 2c) and cubes (Fig. 2e) with the gradual increase of the $FeCl_3$ concentration. The cubes are attributed to be transformed from raft-like precursors or aggregation of nanorods. The product containing both rods and cubes (Fig. 2d) is an intermediate step of turning from rods to cubes, suggesting that the precursor morphologies change from sphere to rod to cube with the increase of C_{FeCl_3}. This transformation is like that observed by Pu et al.[33]. When $C_{CTAB} = 0.04M$ and the iron chloride amount is increased to 0.07 M, that is, $C_{FeCl_3}/C_{CTAB} = 0.07/0.04$, the product still consists of nanocubes, and some of them are broken (Fig. 2f). When the iron chloride concentration is decreased to $C_{FeCl_3} = 0.03M$ while $C_{CTAB} = 0.04M$ ($C_{FeCl_3}/C_{CTAB} = 0.03/0.04$), the perfect cubic-shaped structures of Fe_2O_3 are destroyed, the sample contains non-uniform polyhedral particles, and the particle sizes are less than one micrometer.

Consequently, when the $FeCl_3$ concentration is low, sphere-like β-FeOOH precursors of several nanometers and capped completely by CTAB are formed and transformed into sphere-shaped α-Fe_2O_3 during precursor dissolution/reprecipitation. By increasing the amount of $FeCl_3$ to moderate, α-Fe_2O_3 nanorods form via the transformation of rod-like β-FeOOH precursors. When the $FeCl_3$ concentration is high, the precursors turn to larger raft-like particles, which aggregate and transform to cubic-shaped α-Fe_2O_3particles. These results indicate that the shapes of the β-FeOOH precursors have a significant effect on the morphologies of the synthesized α-Fe_2O_3, and CTAB plays an important role in mediating the hydrolysis of $FeCl_3$. CTAB-the cationic surfactant-capping agents can confine the growth of iron(III) oxides in the nanometer regime. The concentration ratios of raw materials $FeCl_3$ and CTAB (C_{FeCl_3}/C_{CTAB}), the sample names, and the preparation conditions are listed in Table 2.

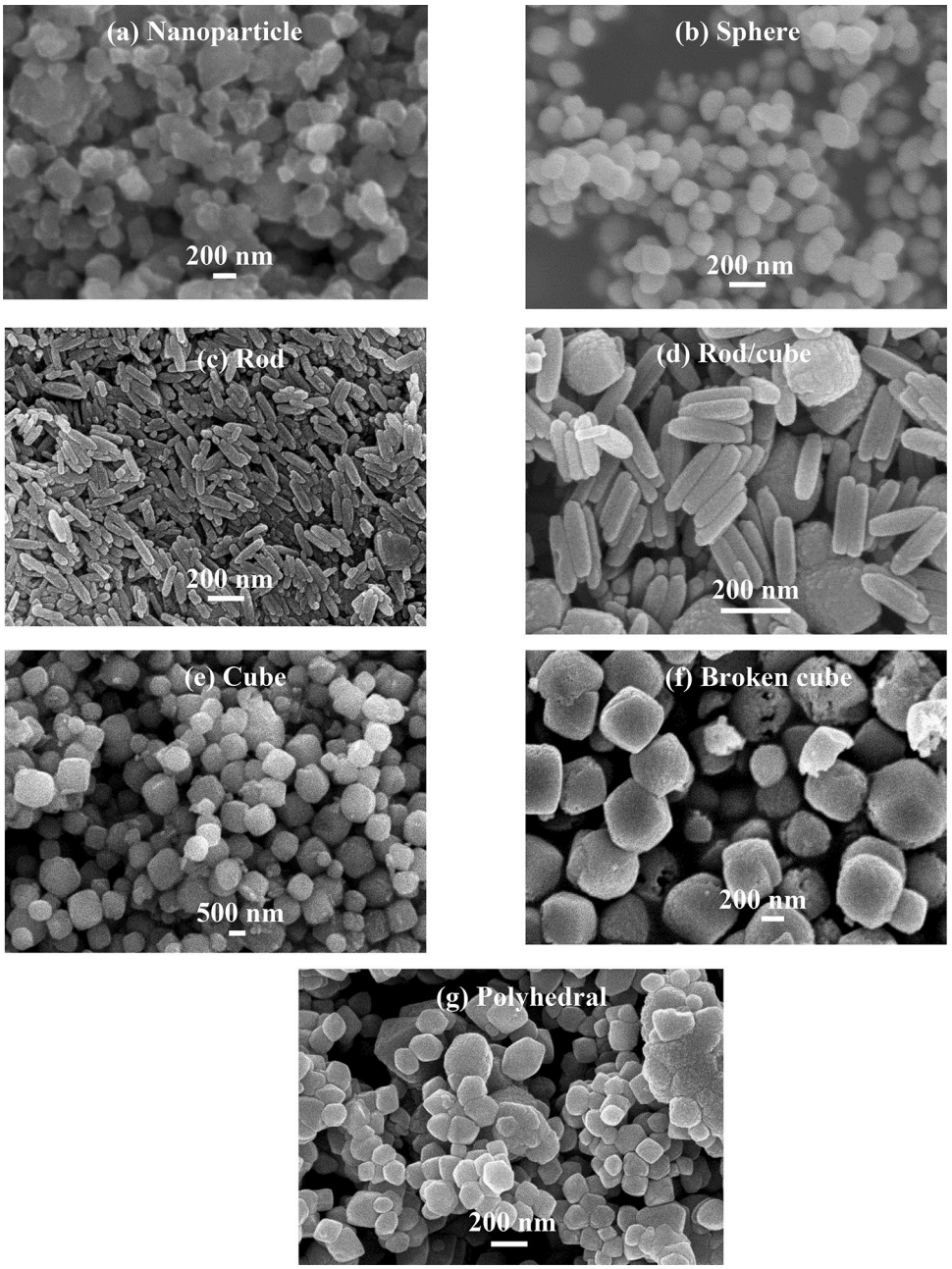

Figure 2. SEM images of the α-Fe_2O_3 materials synthesized at various concentration ratios of $FeCl_3$ and CTAB: (**a**) C_{FeCl_3}/C_{CTAB} = 0.02/0.0(nanoparticle), (**b**) 0.02/0.01(sphere), (**c**) 0.05/0.01 (rod), (**d**) 0.05/0.02 (rod/cube), (**e**) 0.05/0.04 (cube), (**f**) 0.07/0.04 (broken cube), (**g**) 0.03/0.04 (polyhedral).

No.	Sample names	Concentration ratios of precursors (C_{FeCl_3}/C_{CTAB})	Hydrothermal treatment
1	Nanoparticle	C_{FeCl_3}/C_{CTAB} = 0.02/0.0	120 °C—14 h, pH 10
2	Sphere	C_{FeCl_3}/C_{CTAB} = 0.02/0.01	120 °C—14 h, pH 10
3	Rod	C_{FeCl_3}/C_{CTAB} = 0.05/0.01	120 °C—14 h, pH 10
4	Rod/Cube	C_{FeCl_3}/C_{CTAB} = 0.05/0.02	120 °C—14 h, pH 10
5	Cube	C_{FeCl_3}/C_{CTAB} = 0.05/0.04	120 °C—14 h, pH 10
6	Broken cube	C_{FeCl_3}/C_{CTAB} = 0.07/0.04	120 °C—14 h, pH 10
7	Polyhehral	C_{FeCl_3}/C_{CTAB} = 0.03/0.04	120 °C—14 h, pH 10

Table 2. Preparation conditions and samples synthesized via hydrothermal route.

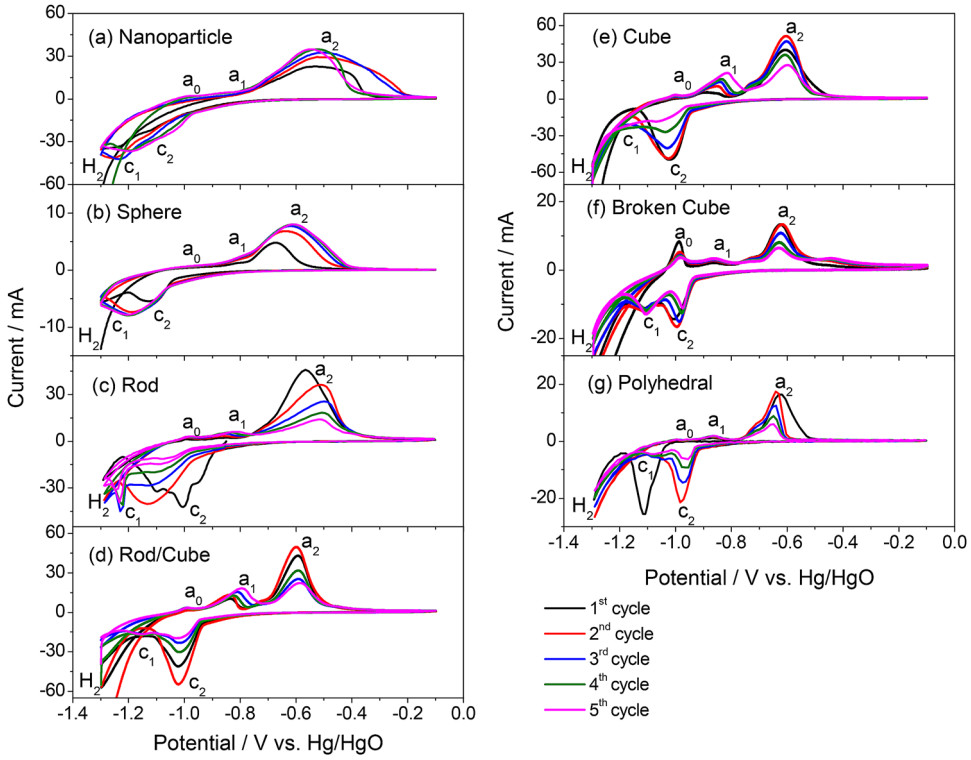

Figure 3. CVs of Fe_2O_3/AB electrodes with various morphologies of Fe_2O_3 synthesized via hydrothermal route in KOH solution: (**a**) nanoparticle, (**b**) sphere, (**c**) rod, (**d**) rod/cube, (**e**) cube, (**f**) broken cube, and (**g**) polyhedral.

In this case, the hydrothermal parameters, namely, pH value, time, and temperature reaction, were kept constant with the changing concentrations of the raw materials, namely, C_{CTAB} and C_{FeCl_3}. In the presence of CTAB, α-Fe_2O_3 nanoparticles with different shapes were obtained when C_{FeCl_3} was changed. When $C_{FeCl_3} = 0.02$, α-Fe_2O_3 nanospheres formed. The shapes of the synthesized α-Fe_2O_3 turned to rods (Fig. 2c) and then cubes (Fig. 2e) with the gradual increase of the $FeCl_3$ concentration. When CTAB was not used, the particles grew randomly to form nanoparticles with different shapes and sizes (Fig. 2a). At $C_{FeCl_3} = 0.02$, α-Fe_2O_3 nanospheres appeared when $C_{CTAB} = 0.01$. When the CTAB concentration was increased to 0.04 and $C_{FeCl_3} = 0.05$, the morphologies of α-Fe_2O_3 changed from spheres to rods and then to cubes. When $C_{CTAB} = 0.04$, the morphology of the α-Fe_2O_3 particles changed to imperfect cubes, that is, broken (Fig. 2f) or polyhedral (Fig. 2g) cubes, with the further increase or decrease of the $FeCl_3$ concentration. This result confirms that CTAB can confine the growth of synthesized products in the nanometer regime, while the $FeCl_3$ concentration can change the shape of the α-Fe_2O_3 nanoparticles. These results are consistent with those in the literature[33]. Therefore, the morphological characteristics of α-Fe_2O_3 are controlled by changing the concentration of raw materials. The synthesized α-Fe_2O_3 nanoparticles with various morphologies can be applied in various technologies. The α-Fe_2O_3 particles with perfect cubic-shaped structures are expected to improve the electrochemical properties of the iron-based battery anode.

The cyclic voltammetry (CV) measurements of the Fe_2O_3/AB electrodes in base electrolyte were taken to investigate the electrochemical properties of the α-Fe_2O_3 materials fabricated via a hydrothermal route, and the results are presented in Fig. 3. The CV profiles of the samples are similar, except that of the Fe_2O_3/AB electrodes using the Fe_2O_3 nanoparticle obtained at $C_{FeCl_3}/C_{CTAB} = 0.02/0.0$ (Fig. 3a). The CV results of the samples depict two pairs of redox peaks, namely, Fe/Fe(II) (a_1/c_1) and Fe(II)/Fe(III) (a_2/c_2), observed at approximately − 0.8 V (a_1)/ − 1.1 V (c_1) and − 0.6 V (a_2)/ − 1.0 V (c_2). Anodic peaks a_1 and a_2 can be attributed to the oxidation of Fe to Fe(II) and Fe(II) to Fe(III), while cathodic peaks c_2 and c_1 correspond to the reduction of Fe(III)/Fe(II) and Fe(II)/Fe, respectively. Thus, a_1 and c_1 correspond to the Fe/Fe(II) redox couple (Eq. 1), while a_2 and c_2 correspond to the Fe(II)/Fe(III) redox couple (Eqs. 2 or 3). Furthermore, we also observed a small oxidation peak (a_0) around − 1.0 V and hydrogen evolution around − 1.2 V. According to Cerny et al.[15], the first oxidation peak (a_0) corresponds to iron oxidation to form $[Fe(OH)]_{ads}$ before $Fe(OH)_2$ is produced. Oxidation peak a_2 is relatively larger and broader than a_1, especially for the Fe_2O_3 nanoparticles (Fig. 3a), and the redox current under the a_2/c_2 couple is higher than that under the a_1/c_1 couple, suggesting that anodic peak a_2 covers the oxidation of the Fe/Fe(II) and Fe(II)/Fe(III) couples. Remarkably, the reduction peaks (c_1) of the Fe_2O_3/AB electrodes with Fe_2O_3 nanoparticles (Fig. 3a) and sphere (Fig. 3b) are completely covered by hydrogen evolution peaks, which may result in low charge efficiency.

Further cycling, the oxidation peaks shifted toward a more positive potential, while the reduction peaks moved toward a more negative potential with the Fe_2O_3 nanoparticles (Fig. 3a), sphere (Fig. 3b), and rod (Fig. 3c)

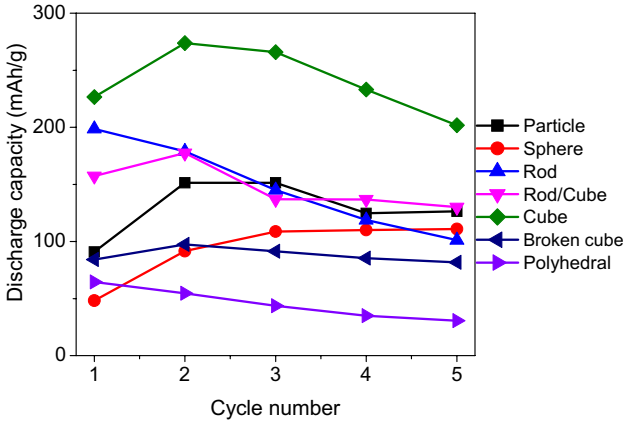

Figure 4. Discharge capacities of Fe_2O_3/AB electrodes in KOH solution.

samples; this shift increased the overpotentials, leading to the disappearance of redox peaks. In contrast, the overpotentials gradually decreased with the Fe_2O_3 rods/cubes (Fig. 3d), cubes (Fig. 3e), broken cubes (Fig. 3f), and polyhedral particles (Fig. 3g). The increase in overpotential may cause negative effects on the capacity and cycling efficiency of Fe_2O_3/AB electrodes. In addition, the redox currents of the electrodes with Fe_2O_3 nanoparticles (Fig. 3a) and sphere (Fig. 3b) increased upon cycling and decreased with the remaining Fe_2O_3 samples (Fig. 3c–f).

The CV profiles of the electrodes with Fe_2O_3 rode/cube, cube, broken cube, and polyhedral samples are similar (Fig. 3d–g); for instance, the redox current increased and then decreased, and their reduction peaks (c_1) are separated from the hydrogen evolution peaks. This behavior is quite different from that of the Fe_2O_3 nanoparticle and sphere samples (Fig. 3a,b), that is, the redox current gradually increased, and their reduction peaks (c_1) disappeared. In contrast, the Fe_2O_3 rod (Fig. 3c) seems to be the intermediate state of the two types of CV curves. These CV results are consistent with the observation of the SEM results as evidenced by the Fe_2O_3 rode/cube, cube, broken cube, and polyhedral samples (Fig. 2d–g), which have similar morphologies, while the Fe_2O_3 nanoparticle and sphere samples (Fig. 2a,b) have similar morphologies, and the rod (Fig. 2c) is in intermediate shape. However, the cubic-shaped structures of the Fe_2O_3 in the polyhedral sample (Fig. 2g) are destroyed, exhibiting random polyhedral particle shapes. Therefore, they provide smaller redox peaks (Fig. 3g) than other cubic-shaped Fe_2O_3 samples (Fig. 3d–f). These findings suggest that the morphological characteristics of the Fe_2O_3 synthesized via a hydrothermal route significantly affect the electrochemical properties of Fe_2O_3/AB electrodes.

A comparison of the CV results of all samples Fe_2O_3 nanoparticle, sphere, rod, rod/cube, cube, broken cube and polyhedral shows that cubic-shaped Fe_2O_3 provides better cyclability than the other samples as clearly evidenced by the well-defined redox peaks. This phenomenon is acceptable because the morphological characteristics of iron oxide affect its redox behaviors. At similar cubic shapes, the Fe_2O_3 particles in the electrode are close-packed, and the contact between cubic-shaped Fe_2O_3 and AB should be tighter than that between other-shaped Fe_2O_3 and AB. Thus, the internal resistance of the cubic-shaped Fe_2O_3/AB electrode should be smaller than that of the other-shaped Fe_2O_3/AB electrode. Consequently, the reaction rate of the cubic-shaped Fe_2O_3 particles was higher than that of other-shaped Fe_2O_3 particles. The SEM images of the synthesized Fe_2O_3 materials show that Fe_2O_3 nanoparticles (Fig. 2a), spheres (Fig. 2b), and rods (Fig. 2c) have a smaller size than cubic-shaped Fe_2O_3 (Fig. 2d–g) and thus need more binders to prepare Fe_2O_3/AB electrodes. However, all the electrodes were prepared at the same ratio of Fe_2O_3:AB:PTFE = 45:45:10 wt%. The number of binders was insufficient to tightly bind to iron oxide and the AB particles in the electrodes when a smaller Fe_2O_3 size was used, resulting in the high internal resistance of the Fe_2O_3/AB electrode. Consequently, Fe_2O_3/AB electrodes with Fe_2O_3 nanoparticles, spheres, and rods exhibit a low redox reaction rate, leading to increased overpotentials and unobservable peaks, whereas the cubic-shaped Fe_2O_3 provides better cyclability and observable oxidation peaks (c_1).

Thus, the Fe_2O_3 materials synthesized at different hydrothermal conditions exhibited different morphologies and consequently provided different electrochemical characterizations. In other words, hydrothermal parameters affected the particle sizes and shapes of the Fe_2O_3 materials and strongly influenced their electrochemical properties. Therefore, by changing the preparation conditions, we can control the desired morphologies, sizes, and shapes of the Fe_2O_3 materials to provide the best electrochemical characterizations.

The CV results show that the shape, size, and morphology of the Fe_2O_3 particles strongly affected the electrochemical properties of Fe_2O_3/AB electrodes, and the cubic-shaped Fe_2O_3, including rods/cubes, cubes, and broken cubes, exhibited better cyclability than the Fe_2O_3 nanoparticles, spheres, and rods.

To find the most suitable Fe_2O_3 among the synthesized materials, the discharge capacities of the Fe_2O_3/AB electrodes with all the synthesized Fe_2O_3 were calculated from the CV profiles, and the results are shown in Fig. 4. Among the synthesized materials, the Fe_2O_3 cube provided the largest discharge capacities. This result is acceptable from the perspective that among the cubic-shaped Fe_2O_3, the Fe_2O_3 cubes possessed a perfect cubic shape, whereas the Fe_2O_3 rods/cubes contained rods and the broken cubes fragments of cubes. This result confirms that Fe_2O_3 cube is the most suitable material. However, the discharge capacity of the Fe_2O_3/AB electrode with an Fe_2O_3 cube gradually decreased with repeated cycling. The electrolyte additive was used to overcome this problem.

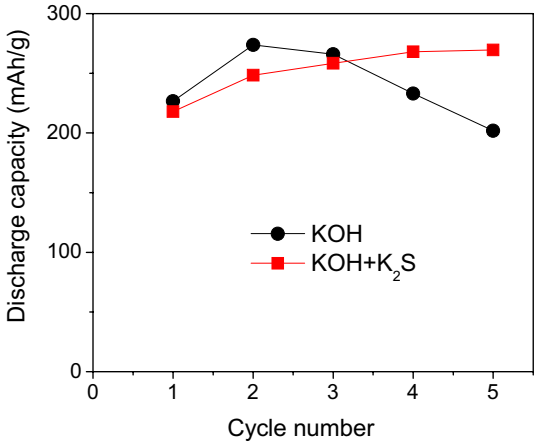

Figure 5. Discharge capacities of Fe_2O_3/AB electrodes with Fe_2O_3 cube in KOH and KOH + K_2S solutions.

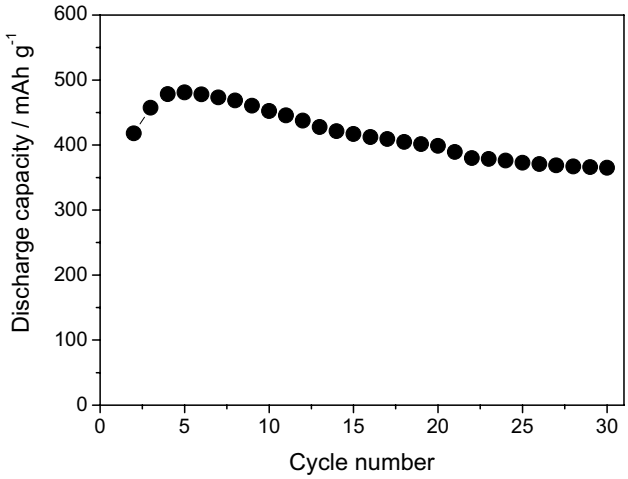

Figure 6. Discharge capacities of Fe_2O_3/AB electrode with cubic-shaped α-Fe_2O_3 in KOH + K_2S solution.

The effects of the K_2S additive on the electrochemical properties of the Fe_2O_3/AB composite electrode were investigated with the Fe_2O_3 cube, showing the highest capacity (Fig. 4), and the result is shown in Fig. 5. The Fe_2O_3 cube sample in the additive electrolyte has larger discharge capacity than that in the base electrolyte. The positive effects of the S^{2-} additive have been reported in previous studies as follows. Ion sulfide is incorporated into the oxide lattice and interacts with Fe(I), Fe(II), or Fe(III) in the oxide film to promote the dissolution of iron[24,28], thus preventing the rapid passivation of iron electrodes during discharge, and increasing the hydrogen evolution overpotential and extending the discharge curve[13,24–29], thereby improving the cyclability and the discharge rates.

The charge–discharge measurement was taken in KOH aqueous solution containing K_2S additive to evaluate the applicability of α-Fe_2O_3 cube materials synthesized via a hydrothermal route in rechargeable batteries. Figure 6 presents the discharge capacities as a function of the number of cycles for the Fe_2O_3/AB electrode using α-Fe_2O_3 cube in the additive electrolyte. The discharge capacities increased from 418 mAh g^{-1} in the first cycle to 457, 478, and 481 mAh g^{-1} in the second, third, and fourth cycles, respectively, and then gradually decreased to 478 mAh g^{-1} in the fifth cycle. The discharge capacity of the Fe_2O_3/AB electrode was approximately 365 $mAhg^{-1}$ at the 30th cycle. Thus, the discharge capacities gradually decreased with the number of cycles. This capacity decline is ascribed to the passivation of the $Fe(OH)_2$ layer formed during the discharge process even in presence of K_2S additive in the electrolyte. Yang et al.[28] investigated sintered iron electrodes and found that the electrode surface is packed closely, and the pores are also filled with the discharge products. In the inner part of the electrode, the discharge products appeared less tightly packed, and a considerable number of pores remained available. They also demonstrated that with small pores, a larger surface of the active material is available for the electrode reaction during discharge. In our case, the Fe_2O_3/AB composite electrode was prepared by pressing a mixture of the Fe_2O_3 particles, AB, and PTFE binder, resulting in high porosity and small pores. It also has a large active material surface for better electrode reaction during discharge. However, capacity decline still occurs and is attributed to the passivation of the $Fe(OH)_2$ layer formed during the discharge process. At the first cycle, the discharged product ($Fe(OH)_2$) is formed on the outer parts of the electrode, and the interior parts of the electrode become inaccessible to the electrolyte. Consequently, the iron oxide particles in the interior of the

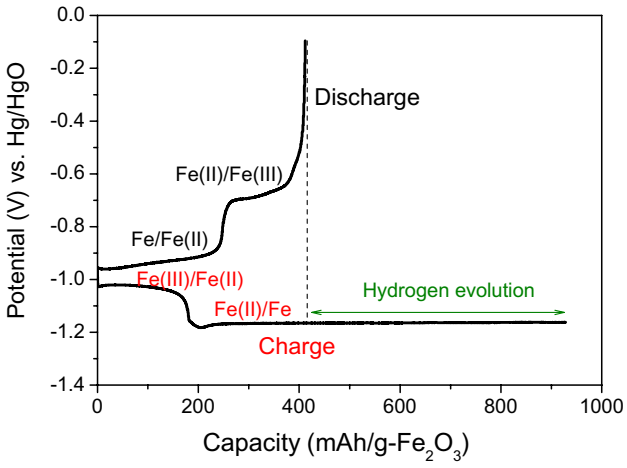

Figure 7. Charge–discharge curves of Fe_2O_3/AB electrode with cubic-shaped α-Fe_2O_3 in KOH + K_2S.

electrode remain under-utilized. Given the small pores of the electrode, in the next cycles, the electrolyte diffuses into the inner parts of the electrode, and redox reactions occur, thereby increasing the capacity. However, the redox reactions of the inner portions of the porous electrodes are poor. With further cycling, the pores are filled with the $Fe(OH)_2$ product, blocking the electrolyte access. Consequently, the capacity gradually decreases.

As mentioned above, when K_2S was added to the electrolyte, S^{2-} additives interacted with Fe(I), Fe(II), and Fe(III) in the oxide film to promote the dissolution of iron, increasing the hydrogen evolution overpotential and prolonging the discharge curve, thereby improving the cyclability and discharge rate of iron electrodes. From the charge–discharge curves, we can estimate the hydrogen evolution produced during the charge and the contribution of the Fe/Fe(II) and Fe(II)/Fe(III) redox couples to the discharge capacity of the electrode. Therefore, the charge–discharge measurement of the Fe_2O_3/AB electrode additive was taken in the additive electrolyte, and the results are shown in Fig. 7.

The charge capacity is much larger than the discharge capacity. Two plateaus are observed at approximately − 0.95 and − 0.70 V (vs. Hg/HgO) in the discharge curves corresponding to the Fe/Fe(II) (Eq. 1) and Fe(II)/Fe(III) (Eqs. 2 and/or 3) reactions, whereas they occur at approximately − 0.95 and − 1.15 V (vs. Hg/HgO) in the charge curves. During the charging process, the valence of iron changes from Fe(III) to Fe(II) and then Fe(II) to Fe. The length of the first and second plateaus in the discharge curves is nearly the same. In the charge curves, the second plateau is longer than the first plateau, suggesting that the second plateau covered the reduction reaction of Fe(II)/Fe (Eq. 1) and hydrogen evolution (Eq. 4). The difference between the discharge and charge capacities is ascribed to the hydrogen evolution reaction. This result demonstrates that hydrogen evolution was only partly suppressed by the S^{2-} additive. The simultaneous hydrogen evolution with the iron deposition reaction results in a low faradaic efficiency during charging and discharge capacity deterioration. Thus, capacity decline is related to the passivation of the $Fe(OH)_2$ formed during the discharge process and the hydrogen evolution reaction during the charge process.

With the further improvement in the capacity retention of Fe_2O_3/AB composite electrodes, the synthesized cubic-shaped α-Fe_2O_3 material can be a potential candidate for energy storage systems. Furthermore, the α-Fe_2O_3 nanoparticles with various morphologies synthesized via a facile hydrothermal route can also be potential materials for other technical applications.

Conclusion

In the present study, various morphologies of α-Fe_2O_3, including nanoparticle, sphere, rod, rod/cube, cube, broken cube, and polyhedral shapes, were successfully synthesized via a facile hydrothermal route in which the morphology is controllable by changing the concentration of raw materials $FeCl_3$ and CTAB. CTAB acts as a surfactant and capping agent and $FeCl_3$ acts as the iron source during synthesis; thus, their concentrations affect the morphological characteristics of the synthesized iron oxides. CTAB can confine the growth of the synthesized α-Fe_2O_3 in the nanometer regime, while the concentration of $FeCl_3$ changes the shape of the α-Fe_2O_3 nanoparticles. By adjusting the concentration ratio of C_{FeCl_3}/C_{CTAB} in the reaction solution, various morphologies of α-Fe_2O_3 materials could be produced. These α-Fe_2O_3 nanoparticles present potential applications in various technological areas.

The investigation of the electrochemical behaviors of the Fe_2O_3/AB composite electrodes using synthesized α-Fe_2O_3 revealed that the morphology, shape, and size of Fe_2O_3 particles strongly affect the performance of Fe_2O_3/AB electrodes. Among the various synthesized α-Fe_2O_3, the cubic shape displayed the highest discharge capacity, but the discharge capacity gradually decreased with prolonged cycling. The K_2S additive in the electrolyte was used to improve the capacity decline. The positive effect of the K_2S additive on the Fe_2O_3/AB electrodes was confirmed by the good cyclability and large capacity of the Fe_2O_3/AB electrodes in the additive electrolyte. Through the optimization of the fabrication conditions and the further improvement in capacity retention, cubic-shaped α-Fe_2O_3 synthesized via hydrothermal treatment is a potential material for iron-based battery

anodes. The controllable synthesis of α-Fe_2O_3 nanoparticles via a facile hydrothermal route is a potential method of producing a large number of nanomaterials for various applications.

Experimental

Synthesis of α-Fe_2O_3 nanoparticles with various morphologies. We prepared α-Fe_2O_3 nanoparticles with different sizes and shapes using the method reported in literature[33] with modifications. The chemicals used in this work, including iron chloride ($FeCl_3.6H_2O$) and cetyltrimethylammonium bromide (CTAB), were of analytical grade. CTAB was used as a surfactant and iron chloride as the iron source. Initially, CTAB aqueous solutions with various concentrations (C_{CTAB}) of 0.01, 0.02, and 0.04 M were prepared by dissolving corresponding CTAB amounts in deionized water, stirring the mixture until the solution became transparent. Iron chloride aqueous solutions with various concentrations (C_{FeCl_3}) of 0.02, 0.03, 0.05, and 0.07 M were prepared using the same process. Then, 80 ml of iron chloride aqueous solution was dissolved in 80 ml of the above CTAB aqueous solution with various concentration ratios of $FeCl_3$/CTAB (C_{FeCl_3}/C_{CTAB}), namely, 0.02/0, 0.02/0.01, 0.05/0.01, 0.05/0.02, 0.05/0.04, 0.07/0.04, and 0.03/0.04. The resultant mixtures were stirred for 60 min to form homogeneous solutions, and the pH value was adjusted to 10 using NH_3 before they were transferred into a Teflon-lined stainless-steel autoclave, sealed, and maintained at 120 °C for 14 h in a typical hydrothermal process. The autoclave was then gradually cooled down to room temperature. The red brown precipitates were collected through centrifugation, washed several times with distilled water and ethanol, subsequently dried at 60 °C for 12 h, and finally annealed at 400 °C for 2 h in air to obtain α-Fe_2O_3 powder.

Characterization. The crystal structure of the synthesized powder was identified using an X-ray diffractometer (XRD; Rigaku) with Cu Kα radiation (k = 0.1542 nm) at 40 kV and 150 mA. The diffraction pattern was recorded in the 2-theta range of 20°–80° with a scanning rate of 5°/min. The morphology and shape of the as-synthesized products were observed by scanning electron microscopy (SEM, JEOL JSM-6060LA/VI, Japan) with an accelerating voltage of 25 kV.

Electrode preparation. The electrode sheet was prepared by mixing 45 wt% synthesized Fe_2O_3 powder as an active material, 45 wt% acetylene black carbon (AB, Denki Kagaku Co.) as an additive, and 10 wt% polytetrafluoroethylene (PTFE; Daikin Co.) binder, followed by rolling. The Fe_2O_3/AB composite electrodes were punched from the electrode sheets into the pellets of 1-cm diameter. The electrode was then pressed onto the conductive Titanium mesh with a pressure of approximately 150 kg cm^{-2}.

Electrochemical measurements. The electrochemical measurements are described in our previous work[32,34]. In this study, we applied the charge current density of 50 mA cm^{-2} instead of 5 mA cm^{-2} in the cycling performance measurement. The details of the electrochemical measurements are as follows. CV and charge/discharge measurements were taken on a three-electrode glass cell assembly with an Fe_2O_3/AB composite as the working electrode, Pt mesh as the counter electrode, and Hg/HgO as the reference electrode. The electrolyte was either a base electrolyte or an additive electrolyte. The base electrolyte was 8 mol dm^{-3} of aqueous KOH solution, and the additive electrolyte was a KOH solution containing 0.01 M K_2S. The CV measurements were taken at a scan rate of 5 mV s^{-1} and within the range of − 1.3 V to − 0.1 V.

For the cycling performance measurement, the galvanostatic process with a cutoff capacity of 1007 mAh g^{-1} Fe_2O_3 was carried out in the charge course. The applied charge current density was 50 mA cm^{-2}. In the discharge course, a constant current density of 2.0 $mAcm^{-2}$ was applied to the electrode with a cutoff potential of − 0.1 V. In all the electrochemical measurements, fresh electrodes were used without precycling.

Received: 30 December 2020; Accepted: 22 February 2021
Published online: 04 March 2021

References

1. Dobley A., Robak J., *Final Report on Research of Air Cathodes for Aluminum Air Batteries*, 16 (2004).
2. Zhang, T., Tao, Z. & Chen, J. Magnesium–air batteries: From principle to application. *Mater. Horiz.* **1**(2), 196–206 (2014).
3. Wang, K. *et al.* Dendrite growth in the recharging process of zinc–air batteries. *J. Mater. Chem. A* **3**(45), 22648–22655 (2015).
4. Higashi, S., Lee, S. W., Lee, J. S., Takechi, K. & Cui, Y. Avoiding short circuits from zinc metal dendrites in anode by backside-plating configuration. *Nat. Commun.* **7**, 11801 (2016).
5. McKerracher, R. D., Ponce de Leon, C., Wills, R. G. A., Shah, A. A. & Walsh, F. C. A review of the iron-air secondary battery for energy storage. *ChemPlusChem* **80**(2), 323–335 (2015).
6. Narayanan, S. R. *et al.* Materials challenges and technical approaches for realizing inexpensive and robust iron–air batteries for large-scale energy storage. *Solid State Ion.* **216**, 105–109 (2012).
7. Manohar, A. K. *et al.* A high-performance rechargeable iron electrode for large-scale battery-based energy storage. *J. Electrochem. Soc.* **159**(8), A1209–A1214 (2012).
8. McKerracher, R. D. *et al.* Improving the stability and discharge capacity of nanostructured Fe_2O_3/C anodes for iron-air batteries and investigation of 1-octhanethiol as an electrolyte additive. *Electrochim. Acta* **318**, 625–634 (2019).
9. Ohmori, H. & Iwai, H. Simulation of solid oxide iron-air battery: Effects of heat and mass transfer on charge/discharge characteristics. *J. Power Sources* **286**, 264–275 (2015).
10. Um, T., Wilke, S. K., Choe, H. & Dunand, D. C. Effects of pore morphology on the cyclical oxidation/reduction of iron foams created via camphene-based freeze casting. *J. Alloy. Compd.* **845**, 156278 (2020).
11. Micka, K. & Zábranský, Z. Study of iron oxide electrodes in an alkaline electrolyte. *J. Power Sources* **19**(4), 315–323 (1987).
12. Vijayamohanan, K., Balasubramanian, T. S. & Shukla, A. K. Rechargeable alkaline iron electrodes. *J. Power Sources* **34**(3), 269–285 (1991).
13. Caldas, C. A., Lopes, M. C. & Carlos, I. A. The role of FeS and $(NH4)_2CO_3$ additives on the pressed type Fe electrode. *J. Power Sources* **74**(1), 108–112 (1998).

14. Chakkaravarthy, C., Perasamy, P., Jegannathan, S. & Vasu, K. I. The nickel/iron battery. *J. Power Sources* **35**, 21–35 (1991).
15. Cerny, K. M. J. Voltammetric study of an iron electrode in alkaline electrolytes. *J. Power Sources* **25**, 111–122 (1989).
16. Salkind, A. J., Venuto, C. J. & Falk, S. U. The reaction at the iron alkaline electrode. *J. Electrochem. Soc.* **111**, 493–495 (1964).
17. Ojefors, L. SEM studies of discharge products from alkaline iron electrodes. *J. Electrochem. Soc.* **123**, 1691–1696 (1976).
18. Armstrong, R. D. & Baurhoo, I. The dissolution of iron in concentrated alkali. *J. Electroanal. Chem.* **40**, 325–338 (1972).
19. Periasamy, P., Babu, B. R. & Iyer, S. V. Cyclic voltammetric studies of porous iron electrodes in alkaline-solutions used for alkaline batteries. *J. Power Sources* **58**, 35–40 (1996).
20. Periasamy, P., Babu, B. R. & Iyer, S. V. Electrochemical behaviour of Teflon-bonded iron oxide electrodes in alkaline solutions. *J. Power Sources* **63**, 79–85 (1997).
21. Hang, B. T. *et al.* The effect of carbon species on the properties of Fe/C composite for metal-air battery anode. *J. Power Sources* **143**, 256–264 (2005).
22. Hang, B. T., Yoon, S., Okada, S. & Yamaki, J. Effect of metal-sulfide additives on electrochemical properties of nano-sized Fe_2O_3-loaded carbon for Fe/air battery anodes. *J. Power Sources* **168**, 522–532 (2007).
23. Manohar, A. K., Yang, C. & Narayanan, S. R. The role of sulfide additives in achieving long cycle life rechargeable iron electrodes in alkaline batteries. *J. Electrochem. Soc.* **162**(9), A1864–A1872 (2015).
24. Ravikumar, M. K., Rajan, A. S., Sampath, S., Priolkar, K. R. & Shukla, A. K. In situ crystallographic probing on ameliorating effect of sulfide additives and carbon grafting in iron electrodes. *J. Electrochem. Soc.* **162**, A2339–A2350 (2015).
25. McKerracher, R. D. *et al.* Effect of 1-octanethiol as an electrolyte additive on the performance of the iron-air battery electrodes. *J. Solid State Electrochem.* **25**(1), 225–230 (2021).
26. Gil Posada, J. O. & Hall, P. J. Post-hoc comparisons among iron electrode formulations based on bismuth, bismuth sulphide, ironsulphide, and potassium sulphide. *J. Appl. Electrochem.* **46**, 451–458 (2016).
27. Wang, Q. & Wang, Y. Overcoming the limiting step of Fe_2O_3 reduction via in situ sulfide modification. *ACS Appl. Mater. Interfaces* **8**, 10334–10342 (2016).
28. Yang, C., Manohar, A. K. & Narayanan, S. R. A high-performance sintered iron electrode for rechargeable alkaline batteries to enable large-scale energy storage. *J. Electrochem. Soc.* **164**(2), A418–A429 (2017).
29. Chamoun, M. *et al.* Stannate increases hydrogen evolution overpotential on rechargeable alkaline iron electrodes. *J. Electrochem. Soc.* **164**(6), A1251–A1257 (2017).
30. Bharathi, S. *et al.* Highly mesoporous α-Fe_2O_3 nanostructures: Preparation, characterization and improved photocatalytic performance towards Rhodamine B (RhB). *J. Phys. D Appl. Phys.* **43**(1), 15501 (2009).
31. Long, N. V. *et al.* Controlled synthesis and characterization of iron oxide micro-particles for Fe-air battery electrode material. *Colloid Polym. Sci.* **293**(1), 49–63 (2014).
32. Hang, B. T., Anh, T. T. & Thang, D. H. Effect of morphology on the electrochemical properties of Fe/C composite electrode as Fe-air battery anode. *J. Nanosci. Nanotechnol.* **16**(8), 7999–8006 (2016).
33. Pu, Z., Cao, M., Yang, J., Huang, K. & Hu, C. Controlled synthesis and growth mechanism of hematite nanorhombohedra, nanorods and nanocubes. *Nanotechnology* **17**(3), 799–804 (2006).
34. Hang, B. T., Thang, D. H., Nga, N. T., Minh, P. T. L. & Kobayashi, E. Nanoparticle Fe_2O_3-loaded carbon nanofibers as iron-air battery anodes. *J. Electrochem. Soc.* **160**(9), A1442–A1445 (2013).

Acknowledgments

This research was funded by Vietnam National Foundation for Science and Technology Development under Grant number 103.02-2018.04.

Author contributions

B.T.H. designed the experiments, analyzed the experimental results and wrote the manuscript. T.T.A. performed the measurements. All authors discussed the research and reviewed the manuscript.

Competing interests

The authors declare no competing interests.

Additional information

Correspondence and requests for materials should be addressed to B.T.H.

Reprints and permissions information is available at www.nature.com/reprints.

Publisher's note Springer Nature remains neutral with regard to jurisdictional claims in published maps and institutional affiliations.